J Solid State Electrochem (2012) 16:625–632
DOI 10.1007/s10008-011-1388-6

ORIGINAL PAPER

Photocatalytic degradation of methyl orange on arrayed porous iron-doped anatase TiO_2

Jianfei Lei · Xiaoping Li · Weishan Li · Fengqiang Sun · Dongsheng Lu · Yuli Lin

Received: 15 November 2010 / Revised: 20 March 2011 / Accepted: 22 March 2011 / Published online: 4 May 2011

Abstract Arrayed porous iron-doped TiO_2 was prepared by sol–gel with polystyrene spheres as template and used as photocatalyst for the degradation of methyl orange. The structure and performances of the prepared photocatalyst were characterized with X-ray diffractometer, inductively coupled plasma-atomic emission spectrometer, scanning electron microscope, UV-visible spectrometer, and methyl orange degradation tests. It is found that the iron dopant does not change the crystal phase of TiO_2 but affects its lattice constant, optical absorption, electronic conductivity, charge-transfer resistance, and activity toward the degradation of methyl orange. The sample doped with 0.01 wt.% Fe (based on Ti) and with smaller pore size exhibits the better photocatalytic activity. The degradation rate of methyl orange on the sample with a pore size of 190 nm is 2.3 times that on the undoped sample with the same pore size.

Keywords Iron-doped TiO_2 · Porous array · Photocatalyst · Degradation · Methyl orange

J. Lei · X. Li · W. Li (✉) · F. Sun · D. Lu · Y. Lin
School of Chemistry and Environment,
South China Normal University,
Guangzhou 510631, China
e-mail: liwsh@scnu.edu.cn

X. Li · W. Li · F. Sun · D. Lu
Key Laboratory of Electrochemical Technology on Energy Storage and Power Generation of Guangdong Higher Education Institutes, South China Normal University,
Guangzhou 510631, China

X. Li · W. Li · F. Sun · D. Lu
Engineering Research Center of Materials and Technology for Electrochemical Energy Storage (Ministry of Education),
South China Normal University,
Guangzhou 510631, China

Introduction

The unique photocatalytic properties of titanium dioxide (TiO_2) have attracted much attention for its application in environmental purification, especially for the degradation of organic compounds [1–6]. However, its practical application is restricted by the band gap energy that limits the utilization of visible light and by the fast recombination of electron–hole pairs generated by band gap excitation. Furthermore, the photocatalytic activity has been handicapped by crystal size and surface morphology of TiO_2. To extend the photoresponse region to visible light and reduce the recombination of electron–hole pairs, many attempts have been made to prepare highly active photocatalysts through various methods including doping [7–12], surface modification [13–15], and narrow band gap semiconductor coupling [16]. Moreover, some novel photocatalysts with controllable crystal size and surface morphology were fabricated to enhance photocatalytic activity through increasing the effective surface area [17–19].

Among various dopants, iron is the most frequently investigated, and many reports have shown that iron-doped TiO_2 exhibits effective photocatalytic activity for degradation of organic pollutants [20–25]. In most studies, however, the doped TiO_2 photocatalysts were used in the form of powders or nanoparticles. There are many disadvantages for the application of these materials, including the difficulty in separation or recovery from the treated water. Attaching the photocatalysts to supporting substrates or preparing immobilized film photocatalysts can overcome the separation problem. The effective surface area is reduced in these operations, resulting in less adsorption of treated substance and thus limiting the photocatalytic efficiency [26, 27]. Therefore, developing new photocatalysts with high activity under visible light irradiation and favorable recycling

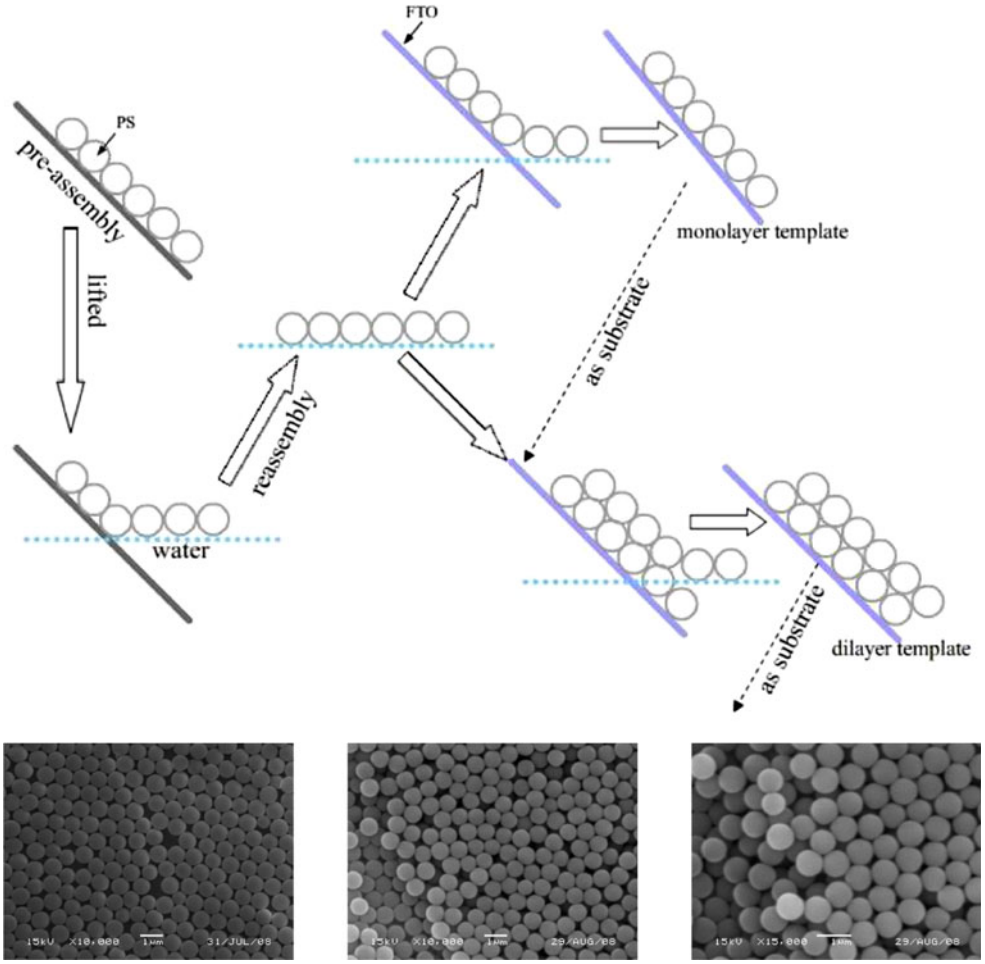

Fig. 1 Schematic illustration for the assembly of PS spheres as template by improved transfer-floating method

characteristics is a challenge for the degradation of organic pollutants. In this regard, arrayed porous doped TiO_2 may be a promising photocatalyst, since this kind of architecture possesses many advantages including high specific surface area and easiness for operating and recycling.

In this paper, the sol–gel method combining template technology was used to fabricate highly active photocatalyst, to arrayed porous iron-doped TiO_2, and its photocatalytic activity was monitored by the degradation of methyl orange (MeO), a common effluent of the textile industry.

Experimental section

Preparation of photocatalyst

Arrayed porous iron-doped TiO_2 photocatalysts were fabricated on a clean F:SnO_2 conductive glass (FTO, R_s=14 Ω/cm^2, Nippon Sheet Glass, Japan) substrate by using polystyrene (PS) spheres as template followed by sol–gel processes. Monodisperse PS spheres (average diameters 850, 580, and 190 nm) were synthesized as previously reported [28], and PS

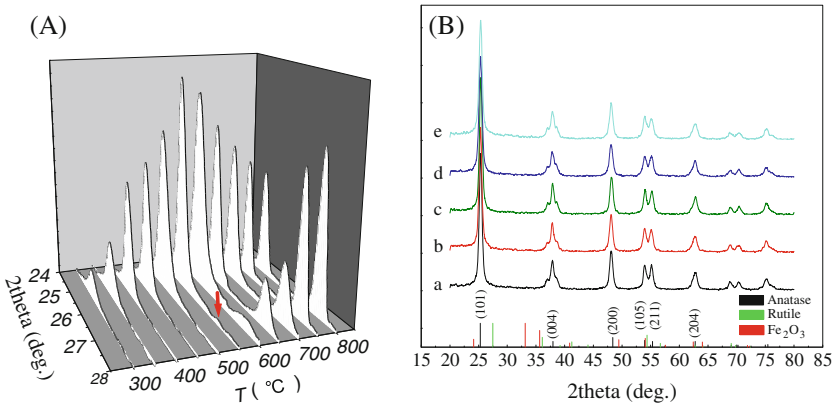

Fig. 2 Thermal evolution of TiO_2 XRD patterns (**a**) and XRD patterns of the samples calcined at 500 °C for 3 h (**b**). The *arrow* indicates the appearance of rutile; *a*: pure TiO_2; *b*: 0.001 wt.% Fe-TiO_2; *c*: 0.01 wt.% Fe-TiO_2; *d*: 0.1 wt.% Fe-TiO_2; *e*: 1.0 wt.% Fe-TiO_2

Table 1 Effects of calcination temperature on phase structure and average crystallite size of TiO_2

	Sample	300 °C	400 °C	500 °C	550 °C	600 °C	700 °C	800 °C
D_A (nm)	Pure TiO_2	8.0	9.7	10.1	12.7	13.0	13.4	17.0
D_R (nm)		–	–	–	0.8	1.4	13.7	18.0

D_A crystallite size of anatase in nanometers, D_R crystallite size of rutile in nanometers

spheres arrayed in a single layer were assembled on FTO by an improved floating-transfer method. Compared with the conventional method [29], this improved method provides an easy way to prepare more regular arrayed PS spheres with controllable layer number, as shown in Fig. 1. Various contents of ferric nitrate were added in the mixture Ti $(OBu)_4$/EtOH/HCl/H_2O/CH_3COOH=1:10:7:2:0.6 in molar to design iron-containing TiO_2 sol. The conductive glass coated with monolayer PS spheres was immersed in iron-containing TiO_2 sol vertically for 2 min to keep the sol filling the template interspace fully under the capillary force. Then, the conductive glass was drawn from the sol vertically with a drawing rate of 4 cm/min and exposed to the air at room temperature for the hydrolysis of titanium ions to form iron-containing TiO_2 gel. Subsequently, the gel was calcined in the oven for 3 h to remove PS template leaving arrayed porous iron-doped TiO_2 on FTO.

Photocatalyst characterization

The crystal structure of the prepared photocatalysts was analyzed with an Analog powder X-ray diffractometer (XRD, Y-2000, China) using Cu-K_α radiation with a scan rate (2θ) of 0.02°/s. Surface morphology was observed with a scanning electron microscope (SEM, JSM-6380LV, Japan). The samples were coated with gold before SEM observation. The content of iron was determined by inductively coupled plasma-atomic emission spectrometer (ICP, IPIS Intrepid IIXSP, USA), and the absorption spectra were recorded using a UV-visible spectrometer (UV-2550PC, Shimadzu, Japan).

Photocatalytic activity measurement

The photocatalytic activity of catalysts was evaluated through the degradation of MeO. Degradation reactions were carried out in a quartz beaker, and a monochromatic light with 369-nm wavelength (incident light intensity, 32 mW/cm^2) was generated from a control intensity photo spectroscope (CIMOS-2, Germany). For each test, the sample with a geometrical area of 0.5 cm^2 was immersed into 10 ml MeO (20 mg/L) solution containing 0.1 M sodium sulfate (Na_2SO_4) as supporting electrolyte. At every given irradiation time, the residual concentration of MeO in the solution was measured with the UV-visible spectrometer at 465 nm which has the maximum absorption of MeO.

Photoelectrochemical performance measurements

Tests of the photoelectrochemical performance were performed on an electrochemical system (Autolab PGSTAT 30, Ecochemie, The Netherlands) combining with the control intensity photo spectroscope. The working electrode was the conductive glass coated with samples, and the counter electrode was a large area platinum foil. A saturated calomel electrode was used as a reference electrode. Electrochemical impedance spectroscopy was measured at the open circuit potential of working electrode with the frequencies from 10^5 to 10^{-1} Hz and the potential amplitude of 10 mV. The resistance is given with respect of the geometrical area of the working electrode. All measurements were conducted in 0.1 M Na_2SO_4 solution.

Results and discussion

Crystal structure, composition, and morphology

TiO_2 has three common crystalline phases: anatase, rutile, and brookite, characteristic of the XRD patterns of (101), (110), and (111), respectively. Figure 2a shows the XRD patterns of arrayed porous TiO_2 calcined at various temper-

Table 2 Composition and structure of iron-doped TiO_2

Samples	Fe (wt.%)[a]	Fe (wt.%)[b]	Crystal phase	Crystal size (nm)[c]
a	0	0	Anatase	10.1
b	0.001	0.0012	Anatase	10.0
c	0.01	0.015	Anatase	9.9
d	0.1	0.14	Anatase	9.0
e	1.0	1.3	Anatase	8.9

[a] Theoretical value
[b] Determined by ICP
[c] Calculated by Debye–Scherrer formula

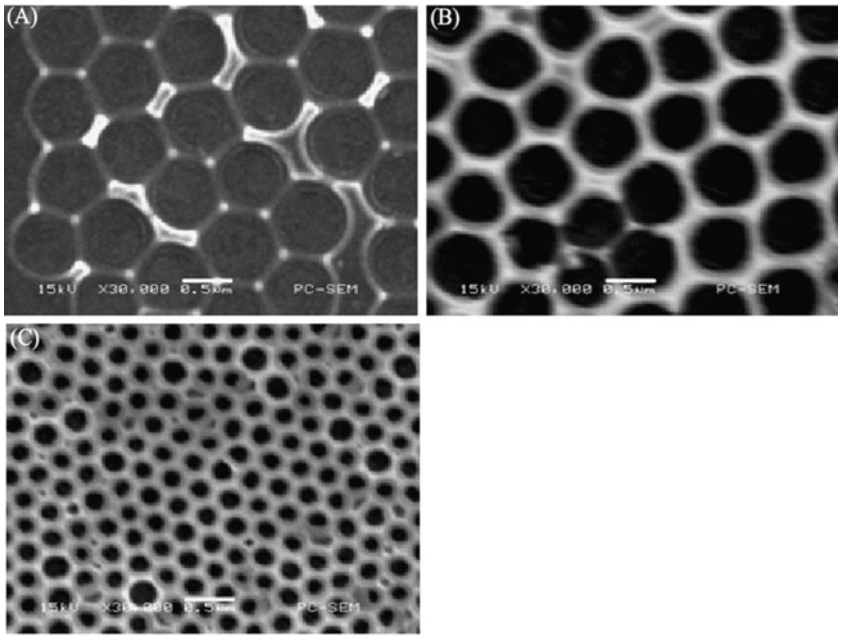

Fig. 3 SEM images of 0.01 wt.% Fe-TiO_2 prepared with 850 (**a**), 580 (**b**), and 190 nm (**c**) PS spheres as template

atures. It can be seen from Fig. 2a that the samples do not contain brookite, only anatase when the temperature is lower than 550 °C, and both anatase and rutile when the temperature is higher than 550 °C. With increasing temperature from 300 °C to 550 °C, the peak intensity of (101) peak increases significantly, and the width of the (101) peak becomes narrower, indicating the growth of anatase phase and the improvement in crystallinity. At 550 °C, the characteristic diffraction peak of rutile phase appears, suggesting that the phase transformation temperature of anatase to rutile was 550 °C. The average crystallite size of the samples calculated by the Debye–Scherrer formula based on the characteristic diffraction peaks is presented in Table 1. It can be seen from Table 1 that, with the increase of calcination temperature from 300 to 800 °C, the crystallite size of anatase increases from 8.0 to 17.0 nm. At 550 °C, rutile begins to form, and its average crystallite size is only 0.8 nm. As the temperature increases further, crystallite size of rutile increases rapidly up to 18.0 nm, while the peak intensity of anatase weakens gradually. It is well known that anatase has best photocatalytic activity among three crystal phases [30]. Therefore, we selected 500 °C as calcination temperature to prepare pure anatase samples for the following tests.

Figure 2b presents the XRD patterns of TiO_2 samples doped with various contents of iron. It can be seen from

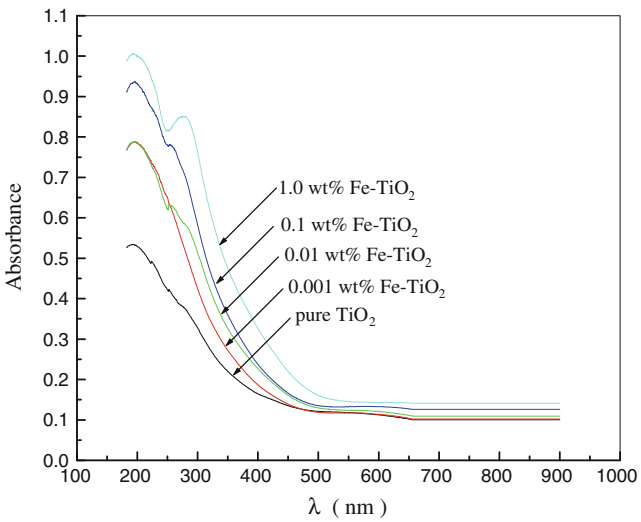

Fig. 4 UV-vis absorption spectra of the samples with a pore size of 190 nm

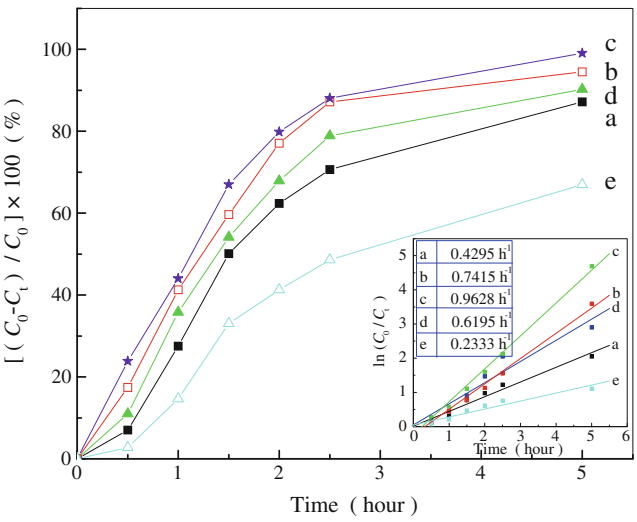

Fig. 5 Degradation efficiency of methyl orange on the samples with a pore size of 190 nm, *a*: pure TiO_2; *b*: 0.001 wt.% Fe-TiO_2; *c*: 0.01 wt.% Fe-TiO_2; *d*: 0.1 wt.% Fe-TiO_2; *e*: 1.0 wt.% Fe-TiO_2

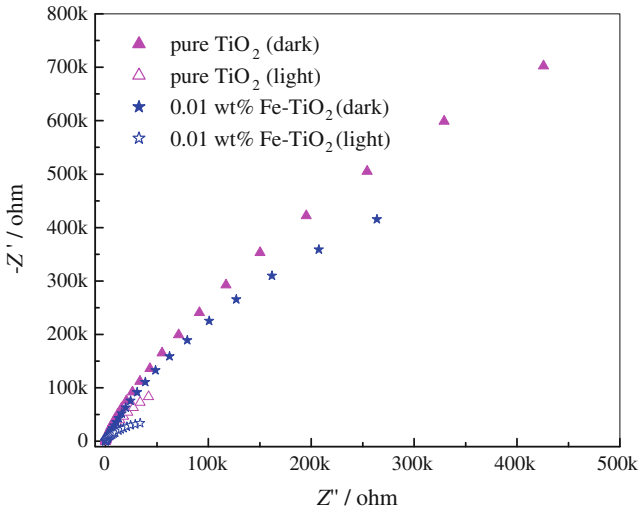

Fig. 6 Nyquist plots of pure TiO_2 and 0.01 wt.% Fe-TiO_2 samples with a pore size of 190 nm in 0.1 M Na_2SO_4

Fig. 2b that only characteristic peak (101) of anatase phase was recorded, indicating that no brookite and rutile phases were formed in all samples. Moreover, it is noteworthy that no crystalline phase attributed to iron oxide can be found in the XRD patterns and the average crystallite size of the samples (shown in Table 2) is reduced due to iron incorporation. This suggests that the doped iron might not exist in a single phase but is substituted for part of Ti^{4+} ions in the crystal lattice of anatase TiO_2. The small amount of iron oxide in the sample might not detected by XRD, but the smaller crystallite size indicates the substitution of iron for titanium. Due to the different ionic sizes, 0.64 Å for Fe^{3+} and 0.68 Å for Ti^{4+}, the substitution of iron ions results in the reduction of the crystal size of TiO_2 [12].

The iron contents in the samples were determined by ICP analysis, and the obtained results are presented in Table 2. It can be seen that the analysis values are almost equal to those added in the solution for the preparation of TiO_2 precursor sol. Therefore, the iron content in TiO_2 can be quantitatively controlled through this sol–gel method.

Figure 3 presents the surface morphology of 0.01 wt.% Fe-TiO_2 samples prepared with three PS spheres (mean diameters 850, 580, and 190 nm). It can be seen that the samples have arrayed porous morphology with the pores arranged uniformly in the distribution of two-dimension. The pore size of samples is approximate to those of PS spheres. Therefore, the pore size of samples can be easily controlled through changing the size of the PS spheres.

UV-vis spectrum

Figure 4 shows the optical absorption spectra of the samples (prepared by 190 nm PS spheres) obtained on the UV-visible spectrometer in the wavelength range of 200–

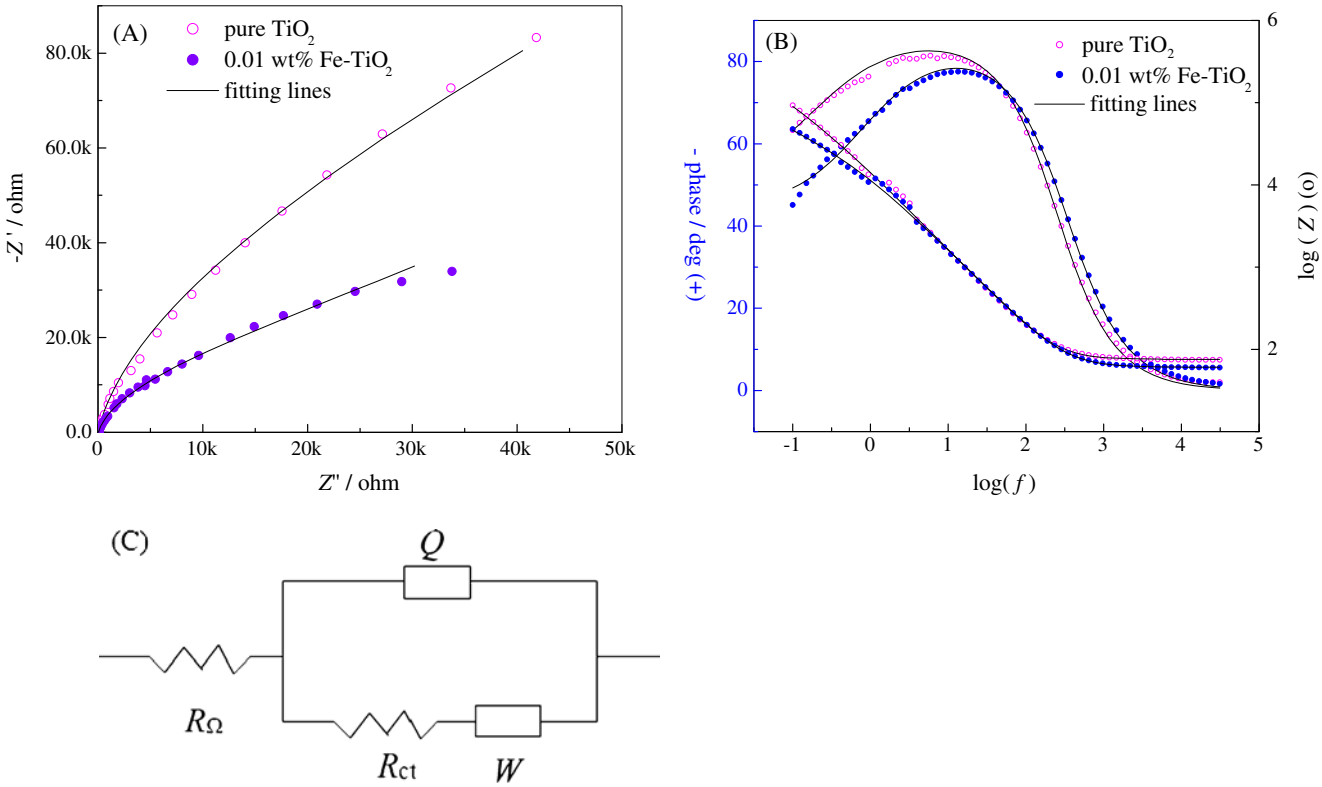

Fig. 7 Modeling of experimental Nyquist (**a**) and Bode (**b**) for the sample with a pore size of 190 nm in 0.1 M Na_2SO_4 under light illumination with the equivalent circuit (*c*). *Dot*: experimental; *solid line*: fitting result

Table 3 Impedance parameters of iron-doped TiO_2 electrode in light illumination

Samples (pore size/nm)	R_Ω (Ω)	R_{ct} (KΩ)
Pure TiO_2 (190)	38	41
0.01 wt.% Fe-TiO_2 (190)	31	11
0.01 wt.% Fe-TiO_2 (580)	32	22
0.01 wt.% Fe-TiO_2 (850)	31	59

R_Ω ohmic resistance, R_{ct} charge-transfer resistance

900 nm. It can be seen from Fig. 4 that the doping of iron in TiO_2 affects the optical absorption band edge and the absorbance of the samples. The optical absorption band edge shifts toward red lights, and the absorbance increases with increasing the content of iron. This result suggests that the doping of iron in TiO_2 can extend the light absorption region to visible light and improve the optical absorption efficiency of the samples.

Photocatalytic activity

Figure 5 shows the effect of the iron content on the photocatalytic efficiency of samples. It can be seen that the doping of iron affects the photocatalytic activity of the arrayed porous TiO_2 toward the degradation of methyl orange. The photocatalytic activity increases with increasing the iron content up to 0.01 wt.%. However, as the iron content increases further, the photocatalytic activity decreases. The degradation rate of methyl orange on the sample with 0.01 wt.% iron is 0.9628 h^{-1}, 2.3 times larger than that on the undoped sample (0.4295 h^{-1}), as shown by the inset of Fig. 5. Obviously, the photocatalyst with 0.01 wt.% iron has the best photocatalytic activity. This phenomenon can be ascribed to the fact that a small amount of iron can act as intermediates for photo-generated hole and electron transportation and inhibit their recombination [31]:

$$TiO_2 + h\nu \rightarrow h^+ + e^- \quad (1)$$

$$Ti^{4+} + e^- \rightarrow Ti^{3+} \quad (2)$$

$$O^{2-} + h^+ \rightarrow O^- \quad (3)$$

$$Fe^{3+} + Ti^{3+} \rightarrow Fe^{2+} + Ti^{4+} \text{ electron trap} \quad (4)$$

$$Fe^{3+} + O^- \rightarrow Fe^{4+} + O^{2-} \quad \text{hole trap} \quad (5)$$

From the viewpoint of crystal field theory, Fe^{4+} and Fe^{2+} ions are relatively unstable compared with Fe^{3+} ions that have half-filled d orbital (d^5). Therefore, there is a tendency for the transfer of the trapped charges from Fe^{4+} or Fe^{2+} to the interface to initiate the following reactions [32]:

$$Fe^{4+} + OH^- \rightarrow Fe^{3+} + OH\bullet \quad \text{hole release} \quad (6)$$

$$Fe^{2+} + O_2 \rightarrow Fe^{3+} + O_2^- \quad \text{electron release} \quad (7)$$

The generated OH• and O^{2-} degrade MeO. As a result, the introduction of Fe^{3+} ions in porous TiO_2 arrays is responsible for reducing the hole–electron recombination rate. On the other hand, a decrease in the activity is expected when

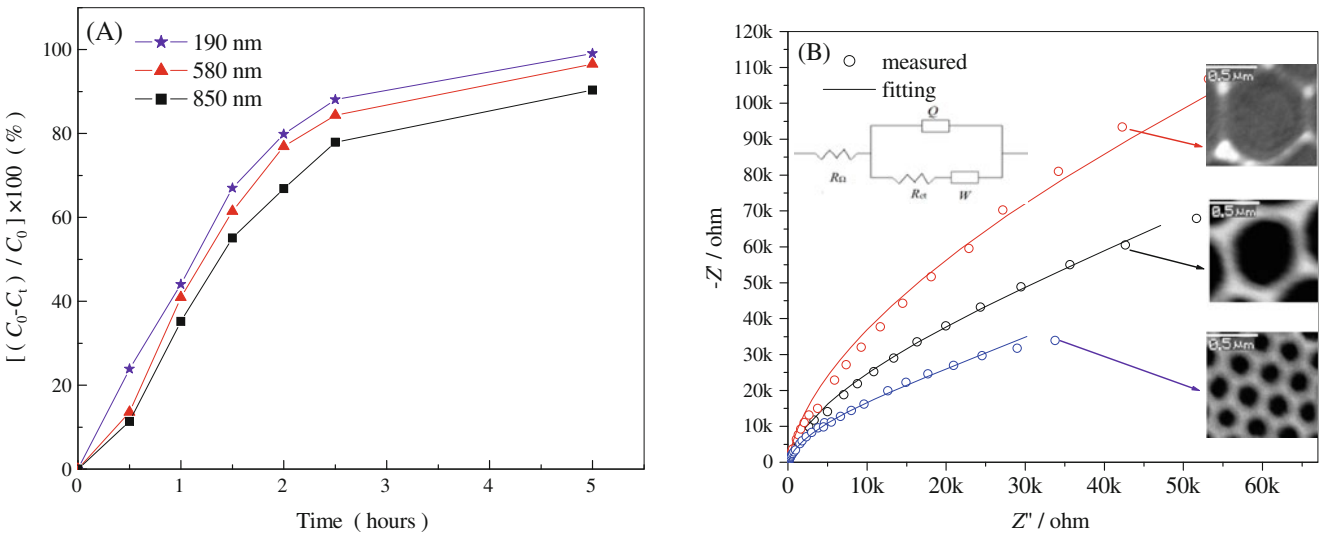

Fig. 8 Degradation efficiency of methyl orange on 0.01 wt.% Fe-doped samples with three pore sizes (**a**) and Nyquist plots and modeling results of three samples (**b**)

the concentration of Fe^{3+} ions becomes too large because the Fe^{3+} can serve not only as a mediator of charge transportation but also as a recombination center. In this study, it can be found that the optimal iron content in TiO_2 is 0.01 wt.%.

Electrochemical impedance spectrum

Figure 6 shows the Nyquist plots of pure TiO_2 and 0.01 wt.% Fe-TiO_2 measured in dark and in light illumination. The Nyquist plots are characteristic of an electrode process mix controlled by charge-transfer and diffusion steps, which is related to the electrode reactions (Eqs. 1, 2, 3, 4, 5, 6, and 7). It can be seen from Fig. 6 that the impedance of two samples is all reduced significantly in light illumination compared with that in dark. The reactions in the electrode are difficult to take place due to the larger energy barrier in dark [33]. Therefore, TiO_2 has larger impedance. In light illumination, the reactions in the electrode take place easily, and thus the impedance is smaller. Under the same conditions, the doped sample has smaller impedance than the undoped sample, suggesting that the iron-doped porous TiO_2 has better photocatalytic activity than the undoped TiO_2.

Figure 7 shows the Nyquist plots (Fig. 7a) and Bode plots (Fig. 7b) together with the modeling results with the equivalent circuit (Fig. 7c) that reflects an electrode process mix controlled by charge-transfer and diffusion steps. In Fig. 7c, R_Ω is associated with ohmic resistance of the system, including solution and TiO_2 resistance. R_{ct} is the charge-transfer resistance and Q is the constant-phase element that reflects the double-layer capacitance on the porous electrode. W is the Warburg impedance reflecting diffusion step. As a photocatalyst, TiO_2 is expected to have low ohmic resistance and low charge-transfer resistance. Table 3 presents the ohmic resistance and the charge-transfer resistance obtained from the fitting.

In the impedance measurements, the distance between working electrode and reference electrode is the same for different tests. Therefore, the difference in R_Ω between different tests reflects the electronic conductivity of TiO_2 samples. It can be seen from Table 3 that R_Ω for 0.01 wt.% Fe-TiO_2 is 31 Ω, smaller than that for pure TiO_2 (38 Ω), indicating that the electronic conductivity of TiO_2 is improved due to the doping of iron. On the other hand, with the doping of iron, R_{ct} decreases from 41 to 11 KΩ, confirming the improved photocatalytic activity of the iron-doped TiO_2.

Effect of the pore size on photocatalytic activity

Three samples with pore size of 850, 580, and 190 nm were used to determine the effect of the pore size on the photocatalytic performance. Figure 8 presents the degradation efficiency of methyl orange on three samples and the obtained Nyquist plots and corresponding fitting results. It can be seen from Fig. 8a that the sample with smaller pore size is more effective for the degradation of methyl orange. The sample with the pore size of 190 nm exhibits the best photocatalytic activity. This result can be confirmed by the electrochemical impedance measurement. Figure 8b presents the Nyquist plots of three samples under light illumination together with the modeling results. It can be found from Fig. 8b that the impedance increases with increasing pore size of the sample. The ohmic resistance and charge-transfer resistance obtained by fitting with equivalent circuit are shown in Table 3. It can be seen from Table 3 that the pore size affects the charge-transfer resistance but hardly affects the ohmic resistance of the samples. The electronic conductivity is an intrinsic property of the samples which is related to the composition and crystal structure but the surface morphology of the samples, therefore the ohmic resistance of the samples with the same composition and crystal phase is almost the same. The charge-transfer resistance depends on the real surface area of the samples, which is related tightly to the surface morphology of the samples. Three samples have the same geometrical areas (0.5 cm^2), but the sample with smaller pore size has larger real surface area. Therefore, the sample with smaller pore size has smaller charge-transfer resistance that results in high photocatalytic activity of the sample.

Conclusion

We reported a new method for the preparation of arrayed porous iron-doped TiO_2 with controllable pore size and iron content and studied the effect of iron content and pore size on the photocatalytic activity for the degradation of methyl orange. In this study, we found that the sample with 0.01 wt.% iron exhibits the best activity. This is because the Fe^{3+} in the sample acts as a mediator of charge transportation when iron content is low but as a recombination center when iron content is too high. The sample with smaller pore size has better activity because of its larger real surface area.

Acknowledgments This work was supported by National Natural Science Foundation of China (NSFC, No.51071071) and Natural Science Foundation of Guangdong Province (Grant No. 10351063101000001).

References

1. Matthews RW (1990) Water Res 24:653–660
2. Ozer RR, Ferry JL (2001) Environ Sci Technol 35:3242–3246
3. Wang RC, Ren DJ, Xia SQ, Zhang YL, Zhao JF (2009) J Hazard Mater 169:926–932

4. Gu L, Chen ZX, Sun C, Wei B, Yu X (2010) Desalination 263:107–112
5. Kumaresan L, Mahalakshmi M, Palanichamy M, Murugesan V (2010) Ind Eng Chem Res 49:1480–1485
6. Tong TZ, Zhang JL, Tian BZ, Chen F, He DN (2008) J Hazard Mater 155:572–579
7. Mei LF, Liang KM, Wang HE (2007) Catal Commun 8:1187–1190
8. Palgrave RG, Payne DJ, Egdell RG (2009) J Mater Chem 19:8418–8425
9. Sasikala R, Sudarsan V, Sudakar C, Naik R, Panicker L, Bharadwaj SR (2009) Int J Hydrogen Energy 34:6105–6113
10. Hamal DB, Klabunde KJ (2007) J Colloid Interface Sci 311:514–522
11. Lu N, Quan X, Li JY, Chen S, Yu HT, Chen GH (2007) J Phys Chem C 111:11836–11842
12. Yu J, Zhou MH, Yu HG, Zhang QJ, Yu Y (2006) Mater Chem Phys 95:193–196
13. Oregan B, Grätzel M (1991) Nature 353:737–740
14. Rajh T, Nedeljkovic JM, Chen LX, Poluektov O, Thurnauer MC (1999) J Phys Chem B Environ 103:3515–3519
15. Ryu J, Choi W (2004) Environ Sci Technol 38:2928–2933
16. Zhang ZH, Yuan Y, Liang LH, Cheng YX, Shi GY, Jin LT (2008) J Hazard Mater 158:517–522
17. Srinivasan M, White T (2007) Environ Sci Technol 41:4405–4409
18. Kontos AI, Likodimos V, Stergiopoulos T, Tsoukleris DS (2009) Chem Mater 21:662–672
19. Ao YH, Xu JJ, Fu DG, Yuan CW (2008) Electrochem Commun 10:1812–1814
20. Zhu J, Ren J, Huo YN, Bian ZF, Li HX (2007) J Phys Chem C 111:18965–18969
21. Kumbhar A, Chumanov G (2005) J Nanopart Res 7:489–498
22. Teoh WY, Amal R, Madler L, Pratsinis SE (2007) Catal Today 120:203–213
23. Zhu JF, Chen F, Zhang JL, Chen HJ, Anpo M (2006) J Photochem Photobiol A 180:196–204
24. Yamashita H, Harada M, Misaka J, Takeuchi M, Neppolian B, Anpo M (2003) Catal Today 84:191–196
25. Ranea KS, Mhalsikera R, Yinb S, Satob T, Choc K, Dunbarc E, Biswas P (2006) J Solid State Chem 179:3033–3044
26. Zhan SH, Chen DR, Jiao XL, Song Y (2007) Chem Commun 20:2043–2045
27. Zhang HM, Quan X, Chen S, Zhao HM, Zhao YZ (2006) Appl Surf Sci 252:8598–8604
28. Lei JF, Li WS (2009) Acta Phys Chim Sin 25:1173–1178
29. Burmeister F, Schafle C, Keilhofer B, Bechinger C, Boneberg J, Leiderer P (1998) Adv Mater 10:495–497
30. Wang J, Ma T, Zhang ZH, Zhang XD, Jiang YF, Pan ZJ, Wen FY, Kang PL, Zhang P (2006) Desalination 195:294–305
31. Yu JC, Ho W, Lin J, Yip H, Wong PK (2003) Environ Sci Technol 37:2296–2301
32. Choi W, Termin A, Hoffmann MR (1994) J Phys Chem 98:13669–13679
33. Li WS, Cai SQ, Luo JL (2004) J Electrochem Soc 151:B220–B226